Single Pt atoms on Ru nanoparticles for CO-resistant methanol oxidation reaction electrocatalysis

Agus Poerwoprajitno
UNSW Sydney
Lucy Gloag
UNSW Australia
John Watt
Los Alamos National Laboratory
Soshan Cheong
UNSW Sydney https://orcid.org/0000-0001-6133-0829
Aaron Henson
North Carolina State University
Bijil Subhash
UNSW Sydney
Nicholas Bedford
UNSW Australia
Benjamin Miller
Gatan Inc
Peter O'Mara
UNSW Sydney
Tania Benedetti
UNSW Australia https://orcid.org/0000-0002-4835-9384
Dale Huber
Sandia National Laboratories
John Gooding
UNSW Sydney https://orcid.org/0000-0002-5398-0597
Wolfgang Schuhmann
Ruhr University Bochum https://orcid.org/0000-0003-2916-5223
Richard Tilley (r.tilley@unsw.edu.au)
UNSW Sydney https://orcid.org/0000-0003-2097-063X

Article

Keywords: single Pt atom catalysts, catalysis, materials science

Posted Date: January 19th, 2021

DOI: https://doi.org/10.21203/rs.3.rs-132040/v1

Version of Record: A version of this preprint was published at Nature Catalysis on March 25th, 2022. See the published version at https://doi.org/10.1038/s41929-022-00756-9.

Abstract

Single Pt atom catalysts on non-active carbon supports have been key targets for electrochemical reactions because the high exposure of active Pt leads to record-high activities. PtRu alloy catalysts are the most active for the methanol oxidation reaction (MOR) as the Ru atoms decrease CO poisoning of the active Pt. To combine the exceptional activity of single atom Pt catalysts with the benefits of an active Ru support we must overcome the synthetic challenge of forming single Pt atoms on noble metal nanoparticles. We have developed a concept to grow and spreads Pt islands on faceted Ru branched nanoparticles to make single Pt atom on Ru catalysts. By following the spreading process with *in situ* TEM, we show that the formation of single atoms is thermodynamically driven by the formation of strong Pt-Ru bonds and a lowering of surface area. The single Pt atom on Ru catalysts successfully limit CO poisoning during MOR to produce record current density and mass activity over time.

Main

The methanol oxidation reaction (MOR) is the limiting reaction for the direct methanol fuel cell because CO-poisoning prevents high current densities over time[1]. CO poisoning is one of the most significant issues limiting the long-term use of catalysts for reactions such as MOR, ethanol oxidation and formic acid oxidation, where CO intermediates form[2,3]. Pt is the most active MOR catalyst, however CO_{ads} intermediates bind strongly to poison the Pt sites, thus preventing access of methanol to these active sites[4]. CO poisoning occurs by the formation of CO_{ads} bound on top of three Pt atoms in a triangular arrangement[5,6]. As a consequence, single atom catalysts are a promising target to overcome CO poisoning if Pt atoms can be dispersed on a support without formation of these triangular arrangements of Pt atoms.

The PtRu system, especially alloy nanoparticles, have been found to be the most effective for MOR because Ru efficiently adsorbs OH_{ads} that can then combine and strip CO_{ads} on neighboring Pt atoms[1,7–9]. Alloy nanoparticles can give this intimate mixture between Pt and Ru but many Pt atoms are inaccessible for catalysis as they are inside the nanoparticle. To maximize the exposure of active Pt atoms, Pt atoms should be only on the surface of a nanoparticle[2,10]. Additionally, forming single Pt atoms onto a pre-formed nanoparticle support has the advantage that key structural features of the nanoparticle support, such as surface faceting, can be incorporated into the final catalyst[11–15]. We have previously shown that introducing low index facets onto branched Ru nanoparticles leads to high catalytic stability for oxidation reactions[16,17]. Thus, branched Ru nanoparticles should make ideal supports for other oxidation reactions such as MOR. We hypothesize that single Pt atoms on faceted Ru nanoparticle supports will form effective and stable CO resilient MOR catalysts.

Successful syntheses of bi-metallic single atom catalysts have focused on embedding single atoms in the surface of a nanoparticle by low-content alloying[18,19] or galvanic replacement of non-noble metal atoms[20,21]. Here, we present a new synthetic approach for achieving single Pt atoms from Pt islands on

metal nanoparticles. Using atomic resolution *in situ* transmission electron microscopy (TEM) studies, we reveal a spreading process as an effective concept for forming single Pt atom catalysts. The thermodynamically driven rearrangement of Pt islands on the Ru low index facets forms discrete Pt atoms on a Ru nanoparticle surface, as illustrated in Scheme 1. The single Pt atoms on Ru nanoparticles are the first single atom catalysts active for MOR. The single Pt atoms on Ru catalysts in this work achieve a very high resilience to CO-poisoning and generate record-high current density and mass activity.

(see Scheme 1 in the Supplementary Files)

Results

The formation process of single Pt atoms on Ru branched nanoparticles

To synthesize single Pt atoms on Ru nanoparticles, firstly, a controlled amount of Pt was grown as islands onto branched Ru nanoparticles. Pt is grown directly onto the low index faceted Ru branches by the slow reduction of Pt(II) precursor with oleylamine in the presence of pre-formed branched Ru nanoparticles (Supplementary Fig. 1)[17]. The Pt grows on the Ru nanoparticle as 2.5 nm sized Pt islands as shown by the discrete areas of Pt in the TEM images (Fig. 1a and b) and energy dispersive X-ray spectroscopy map (EDX, Supplementary Fig. 2) [22]. The Pt islands on Ru nanoparticles were then annealed at mild heat of 200 °C in a weakly reducing atmosphere of 5% H_2/95% N_2 to remove the amine surfactant from the Ru surface[23]. After annealing, the Pt islands become evenly spread over the Ru nanoparticle surface (Supplementary Fig. 3). The spreading of *fcc*-Pt onto *hcp*-Ru branches is confirmed by the loss of Pt peaks in the X-ray diffraction (XRD) pattern after annealing (Supplementary Fig. 4).

To understand the formation of single atom Pt catalysts from Pt islands, we observe changes in the Pt structure using atomic resolution *in situ* TEM with a fast direct detection counting camera while heating the specimen in a H_2 gas flow, as shown in the Supplementary *in situ* movie. The movie shows the transformation of islands into single atoms during annealing. The changes to an individual island are presented by the still images from the movie, in the box in Fig. 1b and c, and are typical of the process occurring across all islands in the sample.

Prior to heating and gas flow *in situ* in the environmental TEM (ETEM), small Pt islands are connected to the low index facets of the branched Ru nanoparticles by a neck of ~ 2 nm in diameter as can be seen in Fig. 1c (t = 3.0 s, Supplementary *in situ* movie). The islands are stable and remain unchanged under the electron beam irradiation (see Methods). Upon *in situ* heating and H_2 gas flow, the Pt starts to spread across the Ru surface causing the height of the Pt island to decrease from 5.8 to 3.8 nm (Fig. 1c, t = 11.2 s). As the islands continue to decrease in size, the contact between Pt and the Ru nanoparticle surface increases (Fig. 1c, t = 22.3 s). The spreading continues until completion when the islands are no longer observable and Pt is dispersed across the surface of the branched Ru nanoparticle (Fig. 1c, t = 37.2 s). The full real-time spreading process can be seen in the Supplementary *in situ* movie.

Two thermodynamic drivers were revealed for the formation of single Pt atom catalysts by atomic resolution snapshots from the *in situ* movie (Fig. 1d and e). (i) The high surface area of the entire nanoparticle lowered as the island decreases in height and spreads across the Ru surface (Fig. 1d, t = 3.0 s)[24]. (ii) The number of Pt-Ru bonds increases as the Pt island spreads and makes larger contact with the Ru nanoparticle (Fig. 1e, t = 22.3 s). The formation of strong Pt-Ru bonds means that it is more energetically favorable to decrease the high surface area of the Pt islands by spreading, rather than sintering and aggregation as is more commonly observed[25–28]. The Pt-Ru bond formation is supported by the crystallographic alignment of Pt atoms with the atomic arrangement of the *hcp* Ru nanoparticle during the spreading process, as shown in the alignment of spots in the fast Fourier transform (FFT) of the images in Fig. 1d and e (see insets). The FFT of the t = 37.2 s image has only spots for *hcp* Ru indicating that no crystalline Pt remains (Supplementary Fig. 5).

Characterization Of Single Pt Atoms On Ru Branched Nanoparticles

The general branched and faceted morphology of the Ru nanoparticle support is retained after spreading of the Pt islands as shown by the straight edges of the nanoparticles in Fig. 2a. The uniform contrast in the low-resolution dark field STEM image in Fig. 2a indicates that the Pt atoms are evenly spread over the Ru nanoparticle with no observable islands remaining. In the atomic resolution image in Fig. 2b. (top left) the heavier Pt atoms are observable as having brighter contrast while the Ru atoms have a darker contrast. The location of the Pt atoms was illustrated by plotting the intensity of the contrast of the atoms in the STEM image, Fig. 2b (top right). As shown by atomic resolution EDX mapping, the Pt signal is only observed at the edge of the nanoparticle, Fig. 2b (bottom left). The Pt EDX signal distribution, Fig. 2b (bottom right), matches the position of atoms with bright contrast in the dark field STEM image and confirms the identity of the Pt atoms. The real space image of individually resolved and elementally identified Pt atoms has no observable triangular arrangements of Pt atoms that are able to adsorb CO. The STEM images indicate that the Pt atoms are crystallographically aligned and in the same atomic columns as the Ru atoms. The high-resolution STEM image in Fig. 2c shows that the low index $(10\bar{1}0)$ and $(10\bar{1}1)$ facets are retained on the branch surface. These observations are consistent with isolated Pt atoms on faceted Ru nanoparticle structure.

To further understand the arrangement of Pt atoms on the Ru support, extended X-ray absorption fine structure (EXAFS) analysis was performed. The Fourier transform (FT) of Pt L_{III}-edge EXAFS spectra alongside the reference Pt foil spectra is presented in Fig. 2d. The single Pt atom structure across the sample was confirmed by the absence of a Pt-Pt coordination peak, in contrast to a pronounced peak for the reference Pt foil. The peak at 1.6–1.9 Å correlates to zero valent Pt atoms coordinated to oxygen and the peak at 2.5-3 Å to Pt coordinated to Ru. Based on the curve fitting (Supplementary Fig. 6 and Supplementary Table 1), Pt is coordinated to 2.25 ± 0.26 lighter elements (modeled as O) and 5.61 ± 1.02 Ru atoms. This local structural arrangement is consistent with Pt atoms on the surface of a Ru *hcp* lattice in the presence of air. The Ru K-edge X-ray absorption near edge structure (XANES, Supplementary Fig. 7) and EXAFS (Supplementary Fig. 8) demonstrates a close resemblance to bulk Ru (Supplementary

Table 2), suggesting that the Ru branches have similar structural and electronic properties to the bulk. This indicates that the branched Ru nanoparticles maintain their crystallographic integrity after the Pt atoms are spread.

Electrocatalytic performance of Pt atoms on Ru nanoparticles towards MOR

The electrocatalytic performance of single Pt atoms on Ru nanoparticles for MOR was evaluated in 0.1 M $HClO_4$ and 1.0 M CH_3OH. The cyclic voltammograms (CVs) of single Pt atoms on Ru, Pt islands on Ru (Fig. 3a), commercial PtRu, and commercial Pt (Supplementary Fig. 9) their difference in performance for the MOR.

The CVs for both the single Pt atoms on Ru and Pt islands on Ru catalysts have an increase in current on the forward (anodic) scan at 0.4 V as the MOR process begins. The current increases rapidly for the single Pt atoms on Ru catalysts, indicative of a highly active catalyst. Without CH_3OH, no increase in current is observed (Supplementary Fig. 10). The current peaks at a potential of 0.75 V and 0.70 V for the single Pt atoms and Pt islands on Ru catalysts respectively, and then falls due to the adsorption of methanol and intermediates occurs faster than the oxidation process[29,30]. On the reverse (cathodic) scan, an increase in current density that peaks at 0.60 V is observed for the Pt islands on Ru catalysts (blue curve, Fig. 3a). This is due to CO_{ads} oxidizing to CO_2 in the 0.4–0.8 V potential window and is typically observed for MOR catalysts[29].

Cyclic voltammetry of the single Pt atoms on Ru catalysts yielded very high capacitance-corrected current density of 14.3 mA cm_{geo}^{-2} at the relatively low potential of 0.7 V, as can be seen in the forward scan peak (Fig. 3a, red). The single Pt atoms on Ru nanoparticles are the most active MOR catalysts, producing 4.7 times greater current density than commercial PtRu catalysts. The single Pt atoms on Ru nanoparticle catalysts have the highest current density reported to date, see Supplementary Table 3[7,31–33]. The high current density of the single Pt atoms on Ru compared to Pt island on Ru catalysts (3.1 times greater) shows the importance of the single atom structure.

The single Pt atoms on Ru catalysts achieve a high specific activity of 0.75 mA cm^{-2}, which is consistent with other bimetallic Pt-Ru alloys that are state-of-the-art for MOR[1]. The high specific activity of the single Pt atoms on Ru catalysts is due to the bimetallic surface of the nanoparticles where active Pt atoms are neighbored by Ru atoms, as compared with Pt island catalysts[7,31].

A mass activity of 1.58 mA g_{Pt}^{-1} was achieved by the single Pt atoms on Ru nanoparticles, which is the highest reported to date for PtRu MOR catalysts, see Supplementary Table 3. These catalysts maximize the utilization of MOR-active sites by having individual Pt atom catalytic sites at the surface and every Pt atom to give a high mass activity.

The critical defining feature of the CV for the single atom catalyst is the very small size of the oxidation peak between 0.6 and 0.4 V on the reverse scan compared to the forward scan. This differs from Pt

islands and commercial PtRu nanoparticles, which display far more prominent oxidation peaks in the reverse scan between 0.5 V and 0.8 V relative to the peak in the forward scan (Fig. 3a and Supplementary Fig. 9). The oxidation peak in the reverse scan occurs when CO_{ads} is removed from the catalyst surface and is typical of catalysts that suffer from CO poisoning. The relative lack of reverse oxidation peak suggests that there is minimal CO_{ads} blocking the catalyst surface during MOR which is further evidence of the single Pt atom on Ru structure[7,33,34].

The resilience to CO poisoning was quantified by comparing the ratio of the charge density of the forward oxidation peak (I_f) to the reverse oxidation peak (I_b) of the CVs in Fig. 3a. The I_f/I_b ratio of the single Pt atoms on Ru catalyst is 6.3, compared to 2.4, 1.2 and 0.8 for Pt island on Ru, commercial PtRu and Pt catalysts, respectively (Fig. 3b). This is 7.9 times higher than commercial Pt and more than 2.5 times higher than state-of-the-art PtRu catalysts (Supplementary Table 3)[32]. This ratio for the single Pt atoms on Ru catalyst is amongst the highest for any MOR catalyst[7, 31–33,35]. The decreased CO poisoning on the single Pt atoms on Ru catalysts can be correlated to the catalyst structure: i) The single atom catalysts have do not exhibit sites with 3 Pt atoms in triangular arrangements that strongly bind CO_{ads}[5,6]. ii) Pt atoms have neighboring Ru atoms that bind OH_{ads}, which readily combines with and strips any CO_{ads} that is formed[30,36]. The high ratio of I_f/I_b further illustrates that Pt is well dispersed across the branched Ru nanoparticles as single atoms with minimal triangular arrangements of Pt atoms that bind CO.

To further understand the performance of the single Pt atom and Pt island on Ru catalysts, faradaic efficiencies and product analysis were derived at a high potential to invoke maximal CO_{ads} poisoning while providing high turnover conditions (1.3 V vs RHE). The single Pt atoms on Ru catalyst generate exclusively CO_2 (97%) and HCOOH (3%) with no $CH_2(OH)_2$ product (Fig. 3c) with highly suppressed CO_{ads} poisoning (Fig. 3b), which is consistent with the oxidation of methanol by an indirect, non-CO pathway (illustrated in Scheme 1)[30]. The significantly higher faradaic efficiency for the oxidation of methanol to CO_2 by the single Pt atoms on Ru catalyst (78%), compared to the Pt island (14%), commercial PtRu (43%) and commercial Pt (13%) catalysts, shows that the single Pt atoms on Ru nanoparticles are highly efficient MOR catalysts (Fig. 3c). As a result, the single Pt atoms on Ru catalysts are the first single atom catalysts that are active for MOR (Supplementary Table 4)[37–40].

The stability of the single Pt atoms on Ru catalysts was assessed for over 240 min at a potential of 0.6 V vs RHE. After 120 min, the single Pt atoms on Ru nanoparticles presented a steady state current density of 2.74 mA cm^{-2}, compared to 0.21 mA cm^{-2} for the Pt island on Ru and commercial Pt nanoparticles (Fig. 3d). Repeated cycling of the single Pt atoms on Ru catalysts also showed < 10% decrease in activity after 1000 cycles (Supplementary Fig. 11). This stability is favorable compared to other state-of-the-art Pt-Ru catalysts that are assessed at different potentials[7,32]. The single Pt atoms on Ru catalysts remaining active over time is attributed to their high resilience against CO-poisoning. The single Pt atom on Ru catalysts are structurally stable due to the strong Pt-Ru bond that prevent atom migration and sintering of the Pt atoms during catalysis as well as the inherent stability of the low index facets of the

branched Ru supports, as indicated by the low dissolution of Ru during MOR (Supplementary Fig. 11)[16,17]. The structural stability is illustrated by post catalysis TEM (Supplementary Fig. 12) showing no observable change in the single Pt atoms on Ru nanoparticle structure.

Conclusions

In this work, we show a new concept of a spreading process to form single Pt atoms on noble metal nanoparticles from Pt islands. The spreading process, as unlocked by *in situ* TEM, is enabled by two thermodynamic drivers i) the lowering of high surface area of the islands and ii) the formation of strong Pt-Metal bonds. These results illustrate the thermodynamic drivers for the formation of single atom structures that can be applied to a wide range of noble metals, which are some of the most important materials for catalysis.

The single Pt atoms on Ru nanoparticles presented in this work are the first single atom catalyst that show activity for MOR and achieve the highest current density and mass activity of any MOR catalyst reported to date. Our results show that single Pt atoms on noble metals is an important target for catalysis because i) the undercoordinated Pt atoms have a high exposed surface area that is easily accessible to incoming catalytic species, ii) the strong Pt-Metal bonds in crystallographically aligned positions at the surface are stable against rearrangement during catalysis, and iii) the single Pt atom structure enables a non-CO pathway that is resilient to CO-poisoning. These design criteria offer the opportunity for the future development of highly active and stable single atom catalysts.

Methods

Synthesis of Pt atoms on Ru nanoparticles. In a typical synthesis, faceted Ru branched nanoparticles (0.1 mmol)[17] and oleyamine (0.2 mmol, Sigma Aldrich, 70%) were dispersed in 5.0 mL 1-octadecene (Sigma Aldrich, 90 %) in 25 mL 2-neck round-bottom flask. The solution was heated at 180 °C for 30 minutes under nitrogen flow. Platinum (II) acetylacetonate (0.005 mmol, Sigma Aldrich, 97%) was dissolved in 2 mL benzyl ether (Sigma Aldrich, 98%) and slowly injected to the Ru solution a rate of 0.2 mL min^{-1}. The reaction was kept for an hour at 180 °C. The synthesized PtRu nanoparticles were purified by precipitation using a mixture of toluene and ethanol, centrifugation at 1500 rpm for 5 minutes. The nanoparticles were then loaded on 10 mg Vulcan XC carbon (Fuel cell store) in 10 mL hexane and were stirred overnight. The products were collected by centrifugation and stored in a vial. The carbon loaded PtRu branched nanoparticles were heated under 5% hydrogen/nitrogen mix gas at 200 °C for 2 hours. The Pt amount was analyzed by inductively coupled plasma-optical emission spectrometry (ICP-OES) method by digesting sample in *aqua regia* for 1 h at 80°C.

Characterization. TEM samples were prepared by drop-casting a solution of nanoparticles in toluene on a carbon coated copper grid under ambient conditions. The low-resolution TEM analysis was taken on a Phillips CM200 microscope operated at 200 keV. The size was calculated using ImageJ software. The high-resolution TEM, STEM, and EDS analysis were performed on a JEOL JEM-F200 operated at 200 kV

and FEI Titan ETEM with image Cs corrector operating at 300 kV. The statistical analysis measured at least 100 nanoparticles using ImageJ software. Atomic-resolution STEM-EDX mapping was performed on a double-aberration-corrected JEOL JEM-ARM300F2 operated at 300 kV, equipped with dual silicon drift X-ray detectors.

In situ Transmission Electron Microscopy Experiments

In situ heating experiments were performed in a FEI Titan ETEM with image Cs corrector operating at 300 keV equipped with a Gatan K3-IS direct detection counting camera and custom gas delivery cart. Single atom Pt/Ru nanoparticle catalysts were drop cast onto Protochips heating chips with holey carbon substrate and loaded onto an Aduro heating holder. The sample was initially heated to 500 ^{o}C and imaged using bright field mode. We observed no change in the Pt/Ru nanoparticle structure at 500 ^{o}C with a cumulative e^- dose of 3000 $e^-/Å^2$, indicating there are no appreciable effects from the e^- beam. Hydrogen (H_2) gas flow was set to 8 sccm and pressure controlled to 100 torr at the delivery point to the ETEM. The leak valves were then adjusted until a steady column pressure of 10 mbar H_2 was achieved. The sample temperature was then increased by 1 ^{o}C/sec until it reached 700 ^{o}C where it was held for the remainder of the experiment. The video was started using a 5 sec 'lookback' feature to capture the initial stages of transformation and recorded at 10 fps using the full field of view of the K3-IS (5760 x 4092 pixels) at a dose rate of 10.6 $e^-/Å^2/s$. The video presented in the Supplementary Information is the result of aligning and combining 10 frames, resulting in a final video that is 1 fps with a cumulative dose rate of 106 $e^-/Å^2/s$. The video presented in Supplementary Information was then sped up by 2 x for ease of data handling and viewing.

X-ray characterization

The X-ray diffraction (XRD) patterns were collected on an Empyrean-II powder diffractometer (PANalytical, Netherlands) fitted with a 10 mm slit, recorded between 30° and 120°.

X-ray absorption spectroscopy measurements were performed at 10-ID-B of the Advanced Photon Source, Argonne National Laboratory. Samples were spread uniformly across folded Kapton tape for measurements in a fluorescence geometry. Pt L_{III}-edge and Ru K-edge measurements were performed from 200 eV below each edge to ~800 eV above each edge[41]. Data processing, analysis, and modeling was performed using the Demeter software package. Ru EXAFS was performed using scattering contributions from hcp Ru, while Pt EXAFS was modeled using bulk Pt, PtO_2 and/or Pt cluster obtained from established metallic clusters[42].EXAFS modeling of Ru and Pt foils were used to obtain S_0^2 values of 0.76 and 0.83 for all subsequent EXAFS calculations.

Electrochemical measurements. The electrochemical measurements were done in a three-electrode system using Pt mesh and Ag|AgCl|NaCl 3 M as counter and reference electrode, respectively. The working electrode was prepared by drop casting a solution containing nanoparticles on a glassy carbon

surface (0.196 cm^2) electrode. A 2.5 mg single Pt atom sample were dispersed in a solution of 140 µl water, 83 µl isopropanol and 10 µl Nafion and 5 µl of the ink was the dropped on a GDE.

The electrochemically active surface areas (ECSAs) were calculated by Cu under-potential deposition (CuUPD) method. A monolayer of Cu was deposited at 0.2 V for 3 min using 5 mM $CuSO_4$ and in 0.1 M $HClO_4$ and followed linier sweep voltammetry from 0.2 to 0.8 V. The electrocatalytic activity and durability of the nanoparticles was studied by cyclic voltammetry (CV) at 50 mV s-1 in 0.1 M $HClO_4$ and 1 M CH_3OH solution. The electrolyte was collected every 250 cycles during CV and analyzed by ICP-MS to calculate the Ru dissolution. The catalytic performance was compared with commercial 20% PtRu alloy nanoparticles on Vulcan carbon (Fuel cell store).

To perform product analysis, a gas-tight H cell (AIDA Science-Technology Development Co. Ltd) separated with a Nafion exchange membrane (Fuel cell store) was used. 2x2 cm carbon cloth (1071 HCB fuel cell store) was used as working electrode. Before sample loading, carbon cloth was sonicated for 10 min and dried in a 120° C oven. A 5 mg single Pt atom sample was dispersed in 1 mL methanol containing 1% (v/v) Nafion (5% wt). An aliquot of 336 µL of this suspension was cast dropwise onto carbon cloth suspended in air by self-closing tweezer. The cloth was left to dry in air. Pt mesh and Ag|AgCl|NaCl 3 M were used as the counter and the reference electrode, respectively.

Gas products were analyzed using gas chromatography (SRI 8610 C, SRI instrument) with automatic injection of 1.0 mL gas aliquots was taken from the cathode exhaust. Liquid products were analyzed using ^{1}H-NMR (Bruker Avance III HD 400 MHz) with 64 scans and 16 s recycle delay. 500 µL aliquots of electrolyte from the cathode compartment were taken before and after chronoamperometry. The aliquots was mixed with 100 µL of DMSO in D_2O stock solution. The DMSO in D_2O stock solution was prepared by mixing 5.0 µL DMSO with 10 mL D_2O. Product quantification was performed via the internal DMSO standard to determine the concentration of methanol oxidation products.

Calculations

The measured catalytic current was normalized by the surface area of glass carbon electrode (0.196 cm^2), ECSAs calculated from CuUPD, and mass of platinum analyzed by ICP-OES to get geometric activity, specific activity and mass activity, respectively.

The Faradaic efficiency (FE) was calculated as:

$$FE = \frac{n\,x\,F\,x\,z}{Q}\,x\,100\%$$

Where n (mol) is the total product (CO_2 or HCOOH) from the electrochemical cell after 2h chronoamperometry (gas chromatography and NMR data), z is number of electron exchanged, F is

faraday constant (965485 C mol^{-1}) and Q (C) is total charge after 2h chronoamperometry.

Declarations

Acknowledgements

The authors acknowledge funding under the Australian Research Council Linkage grant (L.G., J.J.G. R.D.T., LP150101014), the Australian Laureate Fellowship (J.J.G., FT150100060) and the Discovery Project (R.D.T., DP190102659 and DP200100143). A.R.P. thanks to UNSW Scientia Ph.D. scholarship and development scheme. We also acknowledge support from the Australian Research Council of Centre of Excellence in Convergent Bio-Nano Science and Technology (CE140100036) and Microscopy Australia, as well as the Mark Wainwright Analytical Centre and Electron Microscope Unit at the University of New South Wales. W. S. acknowledges funding by the Deutsche Forschungsge-meinschaft (DFG, German Research Foundation) under Germany´s Excellence Strategy – EXC 2033 – 390677874 – RESOLV. This work was performed, in part, at the Center for Integrated Nanotechnologies, an Office of Science User Facility operated for the U.S. Department of Energy (DOE) Office of Science. Los Alamos National Laboratory, an affirmative action equal opportunity employer, is managed by Triad National Security, LLC for the U.S. Department of Energy's NNSA, under contract 89233218CNA000001. Sandia National Laboratories is a multimission laboratory managed and operated by National Technology & Engineering Solutions of Sandia, LLC, a wholly owned subsidiary of Honeywell International, Inc., for the U.S. DOE's National Nuclear Security Administration under contract DE-NA-0003525. The views expressed in the article do not necessarily represent the views of the U.S. DOE or the United States Government. The use of the K3 IS camera was provided courtesy of Gatan. A.H. was supported by award OISE-1357113 from the U.S. National Science Foundation. XAS measurements were performed at 10-ID-B of the Advanced Photon Source, a U.S. Department of Energy (DOE) Office of Science User Facility operated for the DOE Office of Science by Argonne National Laboratory under Contract No. DE-AC02-06CH11357. 10-ID-B is further supported by the Materials Research Collaborative Access Team and its member institutions. We would like to thank Dr Joshua Wright for his assistance with XAS experiments.

Author Contributions

R.D.T., W.S. and J.J.G. conceived and supervised the project. A.R.P and L.G. designed the experiments and prepared the manuscript. S.C. carried out EDS analysis and atomic resolution HAADF-STEM imaging. A.H. synthesized the nanoparticles. B.S. and N.M.B. carried out EXAFS and XANES analysis. J.W. performed ETEM experiments. B.K.M. helped the *in situ* ETEM analysis. P.B.M. and T. M. B. were involved in the electrochemistry experiments. D.L.H. advised on the synthesis of the nanoparticles. All authors contributed to and commented on this paper.

Data Availability

The findings of this study are available within the paper and its Supplementary Information and Movie. All data are available from the authors upon reasonable request.

References

1 Kakati, N. *et al.* Anode Catalysts for Direct Methanol Fuel Cells in Acidic Media: Do We Have Any Alternative for Pt or Pt–Ru? *Chem. Rev.* **114**, 12397-12429, (2014).

2 Duchesne, P. N. *et al.* Golden single-atomic-site platinum electrocatalysts. *Nat. Mater.* **17**, 1033-1039, (2018).

3 Xiong, Y. *et al.* Single-atom Rh/N-doped carbon electrocatalyst for formic acid oxidation. *Nat. Nanotechnol.*, (2020).

4 Alayoglu, S., Nilekar, A. U., Mavrikakis, M. & Eichhorn, B. Ru–Pt core–shell nanoparticles for preferential oxidation of carbon monoxide in hydrogen. *Nat. Mater.* **7**, 333-338, (2008).

5 Neurock, M., Janik, M. & Wieckowski, A. A first principles comparison of the mechanism and site requirements for the electrocatalytic oxidation of methanol and formic acid over Pt. *Faraday Discuss.* **140**, 363-378, (2009).

6 Cuesta, A. At Least Three Contiguous Atoms Are Necessary for CO Formation during Methanol Electrooxidation on Platinum. *J. Am. Chem. Soc.* **128**, 13332-13333, (2006).

7 Huang, L. *et al.* Shape-Control of Pt–Ru Nanocrystals: Tuning Surface Structure for Enhanced Electrocatalytic Methanol Oxidation. *J. Am. Chem. Soc.* **140**, 1142-1147, (2018).

8 Zhao, M. & Xia, Y. Crystal-phase and surface-structure engineering of ruthenium nanocrystals. *Nat. Rev. Mater.* **5**, 440-459, (2020).

9 Martínez-Prieto, L. M. & Chaudret, B. Organometallic Ruthenium Nanoparticles: Synthesis, Surface Chemistry, and Insights into Ligand Coordination. *Acc. Chem. Res.* **51**, 376-384, (2018).

10 Zhang, T., Walsh, A. G., Yu, J. & Zhang, P. Single-atom alloy catalysts: structural analysis, electronic properties and catalytic activities. *Chem. Soc. Rev.*, (2021).

11 Weiner, R. G., Kunz, M. R. & Skrabalak, S. E. Seeding a New Kind of Garden: Synthesis of Architecturally Defined Multimetallic Nanostructures by Seed-Mediated Co-Reduction. *Acc. Chem. Res.* **48**, 2688-2695, (2015).

12 Zhou, M., Li, C. & Fang, J. Noble-Metal Based Random Alloy and Intermetallic Nanocrystals: Syntheses and Applications. *Chem. Rev.*, (2020).

13 Lu, Q. *et al.* Crystal phase-based epitaxial growth of hybrid noble metal nanostructures on 4H/fcc Au nanowires. *Nat. Chem.* **10**, 456-461, (2018).

14 Hao, X. *et al.* Atomic-Scale Valence State Distribution inside Ultrafine CeO2 Nanocubes and Its Size Dependence. *Small* **14**, 1802915, (2018).

15 Meng, C. *et al.* Atomically and Electronically Coupled Pt and CoO Hybrid Nanocatalysts for Enhanced Electrocatalytic Performance. *Adv. Mater.* **29**, 1604607, (2017).

16 Gloag, L. *et al.* Three-Dimensional Branched and Faceted Gold–Ruthenium Nanoparticles: Using Nanostructure to Improve Stability in Oxygen Evolution Electrocatalysis. *Angew. Chem. Int. Ed.* **57**, 10241-10245, (2018).

17 Poerwoprajitno, A. R. *et al.* Formation of Branched Ruthenium Nanoparticles for Improved Electrocatalysis of Oxygen Evolution Reaction. *Small* **15**, 1804577, (2019).

18 Lin, L. *et al.* Low-temperature hydrogen production from water and methanol using Pt/α-MoC catalysts. *Nature* **544**, 80-83, (2017).

19 Liu, J. *et al.* Integrated Catalysis-Surface Science-Theory Approach to Understand Selectivity in the Hydrogenation of 1-Hexyne to 1-Hexene on PdAu Single-Atom Alloy Catalysts. *ACS Catal.* **9**, 8757-8765, (2019).

20 Marcinkowski, M. D. *et al.* Pt/Cu single-atom alloys as coke-resistant catalysts for efficient C–H activation. *Nat. Chem.* **10**, 325-332, (2018).

21 Hannagan, R. T., Giannakakis, G., Flytzani-Stephanopoulos, M. & Sykes, E. C. H. Single-Atom Alloy Catalysis. *Chem. Rev.* **120**, 12044–12088, (2020).

22 Alinezhad, A. *et al.* Direct Growth of Highly Strained Pt Islands on Branched Ni Nanoparticles for Improved Hydrogen Evolution Reaction Activity. *J. Am. Chem. Soc.* **141**, 16202-16207, (2019).

23 Li, D. *et al.* Surfactant Removal for Colloidal Nanoparticles from Solution Synthesis: The Effect on Catalytic Performance. *ACS Catal.* **2**, 1358-1362, (2012).

24 Wang, C. *et al.* Rational Synthesis of Heterostructured Nanoparticles with Morphology Control. *J. Am. Chem. Soc.* **132**, 6524-6529, (2010).

25 Wei, S. *et al.* Direct observation of noble metal nanoparticles transforming to thermally stable single atoms. *Nat. Nanotechnol.* **13**, 856-861, (2018).

26 Yao, Y. *et al.* High temperature shockwave stabilized single atoms. *Nat. Nanotechnol.* **14**, 851-857, (2019).

27 DeRita, L. *et al.* Structural evolution of atomically dispersed Pt catalysts dictates reactivity. *Nat. Mater.* **18**, 746-751, (2019).

28 Prasai, B. *et al.* Synthesis-atomic structure-properties relationships in metallic nanoparticles by total scattering experiments and 3D computer simulations: case of Pt–Ru nanoalloy catalysts. *Nanoscale* **7**, 8122-8134, (2015).

29 Chung, D. Y., Lee, K.-J. & Sung, Y.-E. Methanol Electro-Oxidation on the Pt Surface: Revisiting the Cyclic Voltammetry Interpretation. *J. Phys. Chem. C* **120**, 9028-9035, (2016).

30 Chen, D.-J. & Tong, Y. J. Irrelevance of Carbon Monoxide Poisoning in the Methanol Oxidation Reaction on a PtRu Electrocatalyst. *Angew. Chem. Int. Ed.* **54**, 9394-9398, (2015).

31 Lu, S. *et al.* One-pot synthesis of PtRu nanodendrites as efficient catalysts for methanol oxidation reaction. *Nanoscale* **9**, 1033-1039, (2017).

32 Zhao, W.-Y. *et al.* Highly Active and Durable Pt72Ru28 Porous Nanoalloy Assembled with Sub-4.0 nm Particles for Methanol Oxidation. *Adv. Energy Mater.* **7**, 1601593, (2017).

33 Xue, S. *et al.* Hexapod PtRuCu Nanocrystalline Alloy for Highly Efficient and Stable Methanol Oxidation. *ACS Catal.* **8**, 7578-7584, (2018).

34 Mancharan, R. & Goodenough, J. B. Methanol oxidation in acid on ordered NiTi. *J. Mater. Chem.* **2**, 875-887, (1992).

35 Wang, Q. *et al.* Manipulating the surface composition of Pt–Ru bimetallic nanoparticles to control the methanol oxidation reaction pathway. *Chem. Commun.* **56**, 2419-2422, (2020).

36 Lee, M. J. *et al.* Understanding the Bifunctional Effect for Removal of CO Poisoning: Blend of a Platinum Nanocatalyst and Hydrous Ruthenium Oxide as a Model System. *ACS Catal.* **6**, 2398-2407, (2016).

37 Zhu, C., Fu, S., Shi, Q., Du, D. & Lin, Y. Single-Atom Electrocatalysts. *Angew. Chem. Int. Ed.* **56**, 13944-13960, (2017).

38 Yang, S. & Lee, H. Atomically Dispersed Platinum on Gold Nano-Octahedra with High Catalytic Activity on Formic Acid Oxidation. *ACS Catal.* **3**, 437-443, (2013).

39 Kamiya, K., Kamai, R., Hashimoto, K. & Nakanishi, S. Platinum-modified covalent triazine frameworks hybridized with carbon nanoparticles as methanol-tolerant oxygen reduction electrocatalysts. *Nat. Commun.* **5**, 5040, (2014).

40 Yang, S., Kim, J., Tak, Y. J., Soon, A. & Lee, H. Single-Atom Catalyst of Platinum Supported on Titanium Nitride for Selective Electrochemical Reactions. *Angew. Chem. Int. Ed.* **55**, 2058-2062, (2016).

41 Ravel, B. & Newville, M. ATHENA, ARTEMIS, HEPHAESTUS: data analysis for X-ray absorption spectroscopy using IFEFFIT. *J. Synchrotron Rad.* **12**, 537-541, (2005).

42 Yang, H., Wang, Y., Edwards, A. J., Yan, J. & Zheng, N. High-yield synthesis and crystal structure of a green Au30 cluster co-capped by thiolate and sulfide. *Chem. Commun.* **50**, 14325-14327, (2014).

Figures

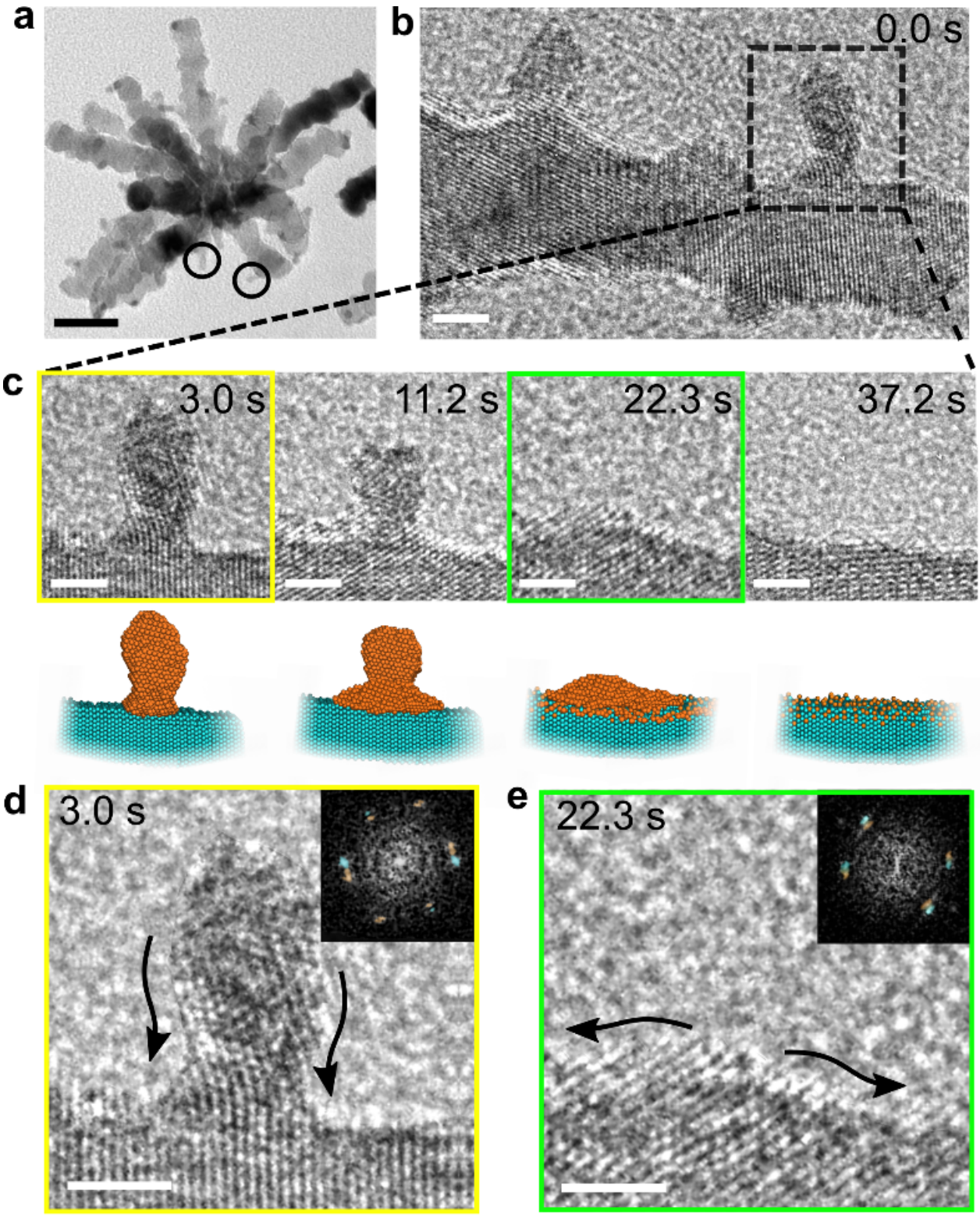

Figure 1

In situ TEM of the spreading process. a. TEM image of an individual nanoparticle consisting of Pt islands on Ru branches. Two examples of typical Pt islands are highlighted by the black circles. Scale bar, 10 nm. b. HRTEM image of the section of Ru branch and Pt island studied for in situ imaging. Scale bar, 2.5 nm

c. HRTEM images and corresponding models of the area in (b) as the nanoparticle is heated under H2 flow in situ. Scale bar, 2.5 nm. d, e. HRTEM images of the Pt branch after 3.0 s and 22.3 s heating under H2 flow. Arrows indicate the migration of Pt atoms. Insets show the corresponding FFTs of the images. Blue highlights the hcp-Ru spots and orange highlights fcc-Pt spots. Scale bars, 2.5 nm.

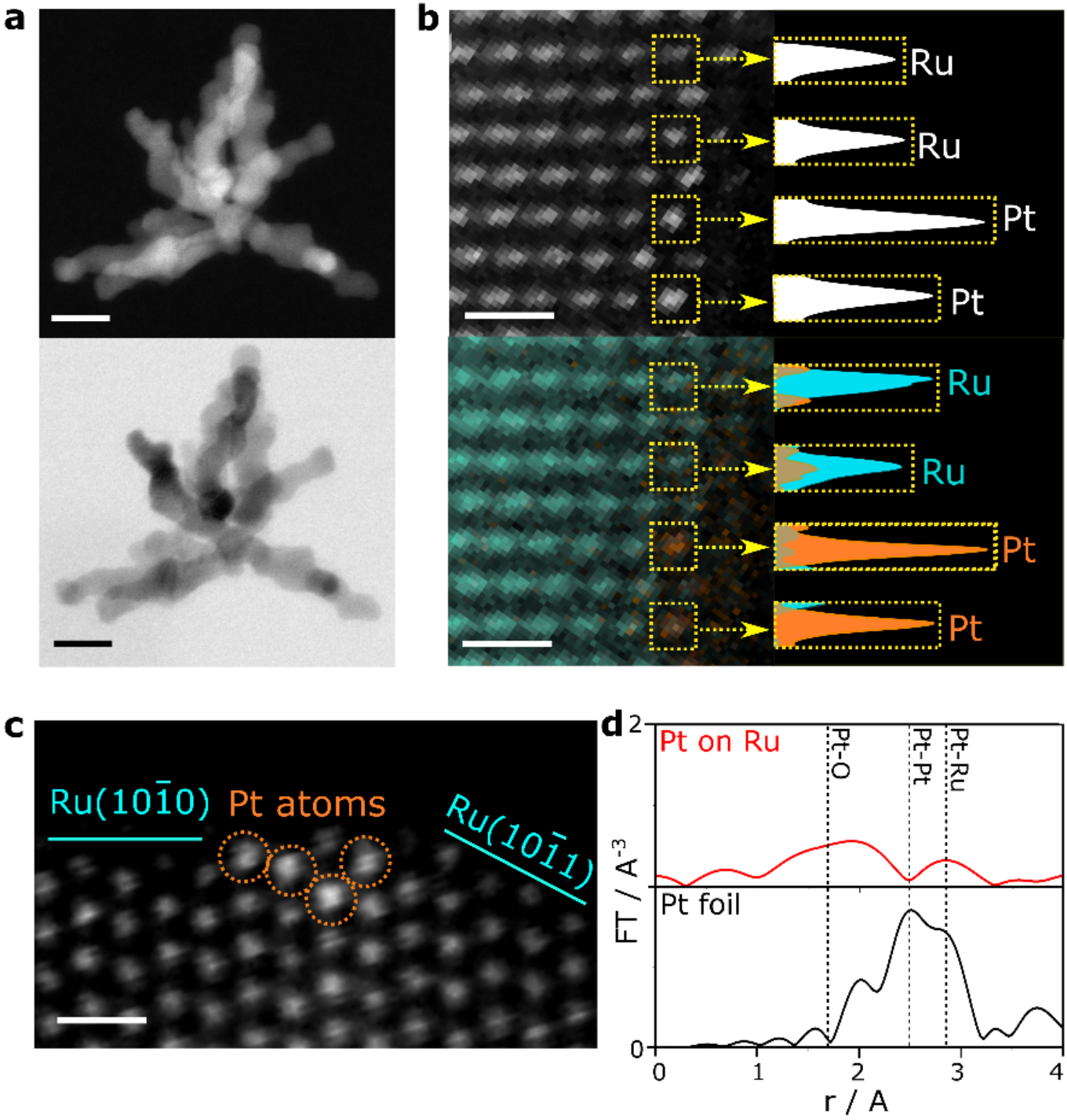

Figure 2

Characterization of the single Pt atoms on Ru nanoparticles. a. Dark field and bright field STEM images of single Pt atoms on Ru nanoparticles. Scale bar, 10 nm. b. HAADF-STEM (top) and EDX mapping (bottom) and their corresponding line scans (yellow boxes) of the location of single Pt atoms (orange) on Ru atoms (blue). Scale bar, 0.5 nm. c. High resolution HAADF-STEM image of the position of Pt atoms in relation to Ru facets. Scale bar, 0.5 nm. e. FT-EXAFS of the Pt LIII-edge spectra of Pt foil (black) and single Pt atoms on Ru nanoparticles (red).

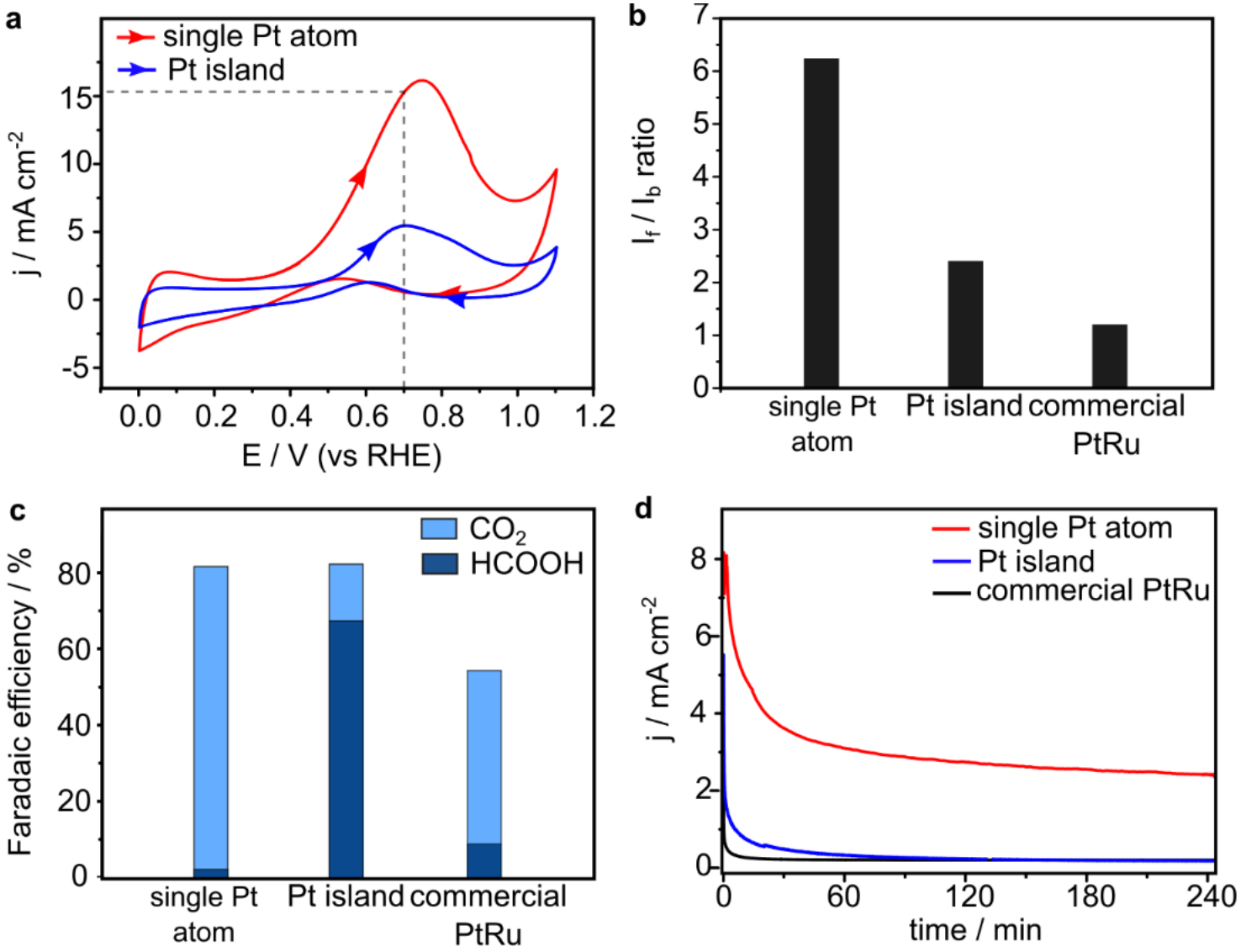

Figure 3

Electrochemical performance for MOR a. Cyclic voltammetry of single Pt atoms on Ru (red) and Pt island on Ru catalysts (blue) in 0.1 M HClO4 and 1.0 M CH3OH. Arrows indicate the direction of the scan. b. Tolerance to CO-poisoning calculated by the charge density of the first forward peak relative to the backward peak (If/Ib). c. Bar plot of the faradaic efficiencies and product analysis obtained at 1.3 V vs RHE. d. Chronoamperometry at 0.6 V vs RHE.

Supplementary Files

This is a list of supplementary files associated with this preprint. Click to download.

- 20201220SIRuPtfinalupload.docx
- Supplementaryinsitumovie.mp4
- Scheme1.pdf